

WPPNets: Unsupervised CNN Training with Wasserstein Patch Priors for Image Superresolution

Fabian Altekrüger^{*†}

Johannes Hertrich[†]

January 21, 2022

Abstract

We introduce WPPNets, which are CNNs trained by a new unsupervised loss function for image superresolution of materials microstructures. Instead of requiring access to a large database of registered high- and low-resolution images, we only assume to know a large database of low resolution images, the forward operator and one high-resolution reference image. Then, we propose a loss function based on the Wasserstein patch prior which measures the Wasserstein-2 distance between the patch distributions of the predictions and the reference image. We demonstrate by numerical examples that WPPNets outperform other methods with similar assumptions. In particular, we show that WPPNets are much more stable under inaccurate knowledge or perturbations of the forward operator. This enables us to use them in real-world applications, where neither a large database of registered data nor the exact forward operator are given.

1 Introduction

Training deep neural networks for solving inverse problems without access to labeled training data is still an active field of research. In inverse problems the task is to reconstruct an unknown ground truth x , e.g. an image, from an observation y generated by

$$y = f(x) + \eta,$$

^{*}Department of Mathematics, Humboldt-Universität zu Berlin, Unter den Linden 6, D-10099 Berlin, Germany, fabian.altekrueger@hu-berlin.de

[†]Institute of Mathematics, Technische Universität Berlin, Straße des 17. Juni 136, D-10623 Berlin, Germany, j.hertrich@math.tu-berlin.de.

with an ill-posed operator f and some noise η . In this paper, we focus on the problem of superresolution. Here, x is a high-resolution image, y a low resolution observation and the forward operator f is a composition of a blur operator and a downsampling operator. The reconstruction of the high-resolution image x from the low-resolution observation y using deep neural networks is considered in many papers, see e.g. [11, 30, 38, 39, 44, 48, 50, 53]. However, within their training process, most of these methods require to have access to a large data base with registered pairs (x_i, y_i) of high- and low-resolution images. Only very few neural network based approaches make use of the forward operator f instead of large training data sets. Examples are plug-and-play methods [47], the zero-shot superresolution [41] and the deep image prior [45], which uses the structure of a convolutional neural network and an early-stopping technique for regularizing the reconstruction x from y . The idea of plug-and-play methods is to consider an optimization algorithm from convex analysis (e.g. the forward-backward splitting [6] or the alternating direction method of multipliers [7, 12]) to solve a variational problem

$$\mathcal{J}(x) = D(x, y) + \lambda \mathcal{R}(x), \quad (1)$$

where $D(x, y)$ is a data-fidelity term and \mathcal{R} a regularizer. Now, plug-and-play methods replace the proximal steps with respect to the regularizer by a powerful denoiser as BM3D [9] or neural networks [43]. Plug-and-Play methods were used for several applications with excellent performance, see e.g. [3, 15, 19, 33, 35, 51]. Closely related to plug-and-play methods are regularizing by denoising (RED) [37], variational networks [13] and total deep variation [26]. Similar to plug-and-play, these methods consider the variational problem (1) and replace the regularizer by some neural network based steps.

Alternatively to neural networks, a wide range of methods based on the self-similarity of small $p \times p$ patches within natural images was developed in the last years. Patch-based methods can be used for several inverse problems as denoising [2, 21, 28] or superresolution [20, 40]. In particular, the expected patch log likelihood algorithm (EPLL) [36, 54] achieved competitive results to neural networks by using the log likelihood function Gaussian mixture model as regularizer within the variational problem (1).

In this paper, we assume that we are given the forward operator f , a data base of low resolution images y_1, \dots, y_m and one single high-resolution reference image \tilde{x} . Further, we assume that the distribution of all $p \times p$ patches in \tilde{x} is similar to the patch distribution in the unknown high-resolution ground truths x_1, \dots, x_m corresponding to y_1, \dots, y_m . This assumption is fulfilled e.g. for textures or images of material data. The setting is motivated by the imaging of materials microstructures. Here, it is usually possible to scan a large

area of a material with a low resolution, while the limited amount of time and resources forbids to image the same size of a data sample using a higher resolution. Further, it is often impossible to scan the same section of one sample twice with different resolutions as in many applications destructive imaging processes, e.g. FIB-SEM are used. These imaging processes destroy the scanned section of the material and consequently there is no chance to generate labeled training data.

The authors of [18] proposed within this setting to solve the variational problem (1) using a regularizer \mathcal{R} , which penalizes the difference between the unknown patch distribution within the reconstruction x and the reference image \tilde{x} . Here the distance between the patch distribution is measured by the Wasserstein-2 distance and the resulting model is called a Wasserstein patch prior. This was inspired by the idea that a texture-like image can be represented by the distribution of all $p \times p$ patches [14, 16, 23, 29], which was used in [23] to synthesize textures by minimizing the Wasserstein distance between the patch distribution in the synthesized image and some reference image. Unfortunately, the minimization of (1) using the Wasserstein patch prior requires several computations and differentiations of Wasserstein distances, which is computationally expensive and therefore intractable for large images.

In this paper, we propose WPPNets, which are convolutional neural networks (CNNs) trained in an unsupervised way using a new loss function based on the Wasserstein Patch Prior from [18]. We establish a relation to maximum a posteriori (MAP) estimators in a Bayesian inverse problem and demonstrate the performance of our method based on several numerical examples using real-world data¹. It turns out that WPPNets outperform comparable methods as plug-and-play methods and the deep image prior. In practice, it is often unrealistic to assume that the forward operator f is known exactly. Instead, it can be described inaccurately or estimated on synthetic data. We demonstrate by some numerical examples that WPPNets are much more stable under such perturbations of the operator than other approaches.

Note that even though we focus on superresolution, the WPPNets could also be applied for other inverse problems. Further, due to the fact that WPPNets require the knowledge of one high-resolution reference image, WPPNets could also be interpreted as a method for one-shot learning, see [5, 49] and references therein. However, as no low-resolution correspondence to the reference image is given, we would call WPPNets an unsupervised learning method.

The paper is organized as follows. In Section 2 we shortly review the Wasserstein patch

¹We provide an implementation of WPPNets online at <https://github.com/FabianAltekrueger/WPPNets>.

priors from [18] and establish a relation to MAP estimators in Section 3. We propose our new loss function for WPPNets in Section 4. Afterwards, in Section 5, we present numerical examples and compare our results with other methods. Lastly, conclusions are drawn in Section 6.

2 Wasserstein Patch Prior

In this section, we introduce a main ingredient of our superresolution model, namely the distance between empirical measures generated from image patches.

Let $P_j: \mathbb{R}^{d_1 \times d_2} \rightarrow \mathbb{R}^{s_1 \times s_2}$, $j = 1, \dots, N$ denote the operator which extracts the j -th patch of size $s_1 \times s_2$ with $s_1 < d_1$, $s_2 < d_2$ from an image in $\mathbb{R}^{d_1 \times d_2}$. Resampling the image columnwise, we may consider $P_j: \mathbb{R}^d \rightarrow \mathbb{R}^s$, where $d := d_1 d_2$ and $s := s_1 s_2$. Based on image patches, we define the *empirical patch distribution* μ_x of an image $x \in \mathbb{R}^d$ as the empirical measure on \mathbb{R}^s given by

$$\mu_x = \frac{1}{N} \sum_{j=1}^N \delta_{P_j x}.$$

The main assumption in the following models is that similarly structured images x and \tilde{x} have also similar empirical patch distributions. As distance between such distributions we use the Wasserstein-2 distance, where we just refer to the Wasserstein distance in the sequel. For empirical measures

$$\mu := \frac{1}{N} \sum_{j=1}^N \mu_j \delta_{p_j}, \quad \tilde{\mu} := \frac{1}{M} \sum_{k=1}^M \delta_{\tilde{p}_k}, \quad p_j, \tilde{p}_k \in \mathbb{R}^s,$$

the Wasserstein distance is defined by

$$W_2^2(\mu, \tilde{\mu}) := \min_{\pi \in \Pi(\mu, \tilde{\mu})} \sum_{j=1}^N \sum_{k=1}^M \|p_j - \tilde{p}_k\|^2 \pi_{j,k}$$

where $\Pi(\mu, \tilde{\mu}) := \{\pi = (\pi_{j,k}) \in \mathbb{R}_{\geq 0}^{N \times M} : \sum_{j=1}^N \pi_{j,k} = \frac{1}{M}, \sum_{k=1}^M \pi_{j,k} = \frac{1}{N}\}$. We will use the dual form of the Wasserstein distance given by

$$W_2^2(\mu, \tilde{\mu}) = \max_{\psi \in \mathbb{R}^M} \left(\frac{1}{N} \sum_{j=1}^N \psi^c(p_j) + \frac{1}{M} \sum_{k=1}^M \psi_k \right), \quad (2)$$

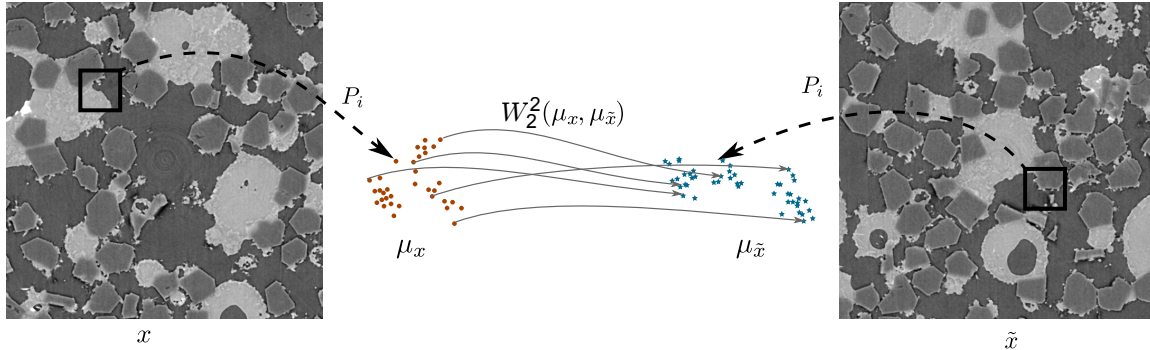


Figure 1: Illustration of the Wasserstein Patch Prior.

where $\boldsymbol{\psi} := (\psi_k)_{k=1}^M$ and $\psi^c(p_j) := \min_{k \in \{1, \dots, M\}} \{\|p_j - \tilde{p}_k\|^2 - \psi_k\}$ denotes the c -transform of $\boldsymbol{\psi}$. Given a template image $\tilde{x} \in \mathbb{R}^{\tilde{d}}$, we intend to approximate the solution $x \in \mathbb{R}^d$ of an inverse problem using the Wasserstein distance $W_2^2(\mu_x, \mu_{\tilde{x}})$ between their patch distributions which we call *Wasserstein Patch Prior* (WPP). Note that only all patches must have the same size, but not the images. Such distances were introduced by Houdard et al. [22] for generating textures and were used in Hertrich et al. [18] as a regularizer within a variational model for solving inverse problems. An illustration is given in Figure 1.

3 MAP Estimation with Wasserstein Patch Prior

Next we recall the variational model with WPP of Hertrich et al. [18], but from a MAP point of view. Let X be a random variable on \mathbb{R}^d with density $p_X(x) \propto \exp(-\mathcal{R}(x))$ for some measurable mapping $\mathcal{R}: \mathbb{R}^d \rightarrow \mathbb{R}$ such that $\exp(-\mathcal{R}(x))$ is integrable. Now, consider the Bayesian inverse problem

$$Y = f(X) + \eta,$$

where $\eta \sim \mathcal{N}(0, \sigma^2 I)$ is independent of X . Then, Bayes' theorem implies that maximizing the log-posterior distribution $\log(p_{X|Y=y}(x))$ can be rewritten as

$$\begin{aligned} \arg \max_x \log(p_{X|Y=y}(x)) &= \arg \max_x \log \frac{p_{Y|X=x}(y) p_X(x)}{p_Y(y)} \\ &= \arg \max_x \left\{ \log \left(\exp \left(-\|f(x) - y\|^2 / (2\sigma^2) \right) \right) + \log(p_X(x)) \right\} \\ &= \arg \min_x \left\{ \frac{1}{2} \|f(x) - y\|^2 + \sigma^2 \mathcal{R}(x) \right\}. \end{aligned}$$

Using the WPP $\mathcal{R}(x) := \rho W_2^2(\mu_x, \mu_{\tilde{x}})$ with $\rho := \frac{\lambda}{\sigma^2}$, we obtain the variational model

$$\mathcal{J}(x) := \frac{1}{2} \|f(x) - y\|^2 + \lambda W_2^2(\mu_x, \mu_{\tilde{x}}). \quad (3)$$

However, minimizing this function can be only interpreted as a MAP maximization if, up to a multiplicative constant, the function $\exp(-\rho W_2^2(\mu_x, \mu_{\tilde{x}}))$ is a probability density, i.e. it has to be integrable. This is ensured by the following proposition which proof is given in the appendix.

Proposition 1. *For $\varphi(x) := \exp(-\rho W_2^2(\mu_x, \mu_{\tilde{x}}))$, it holds $\int_{\mathcal{X}} |\varphi(x)| dx < \infty$.*

In [18] it was shown that the WPP outperforms state-of-the-art methods for the superresolution of material images. However, it requires the minimization of the functional (3) for each high-resolution image x we want to reconstruct from a low resolution image, which is computationally costly. Therefore we propose to learn a neural network based on the above loss function and then to use this network to generate high resolution images in a fast way. In other words, the network will be trained to map an observation y onto the corresponding MAP estimator x of X given $Y = y$ under the prior distribution defined by the density $p_X \propto \varphi$.

4 CNNs Using Wasserstein Patch Priors

We assume that we are given a high-resolution example image $\tilde{x} \in \mathbb{R}^d$ with patch distribution $\mu_{\tilde{x}} = \frac{1}{N} \sum_{k=1}^{\tilde{N}} \delta_{P_k \tilde{x}}$ and several low resolution images $Y = (y_1, \dots, y_m)$, $y_i \in \mathbb{R}^n$. The corresponding high-resolution ground truth images (x_1, \dots, x_m) are unknown, but we assume that the x_i have a similar patch distribution as the reference image \tilde{x} for $i = 1, \dots, m$.

Based on (3) it appears natural to train a CNN G_θ using the loss function

$$\mathcal{L}(\theta) = \frac{1}{m} \sum_{i=1}^m \|f(G_\theta(y_i)) - y_i\|^2 + \lambda W_2^2(\mu_{G_\theta(y_i)}, \mu_{\tilde{x}}). \quad (4)$$

The first summand of \mathcal{L} serves as a data consistency term, enforcing that the reconstructions fit to the low-resolution observation, while the second one ensures the similarity of the patch distributions of the reconstructions to the reference image \tilde{x} . The later assumption is very realistic for large special structured images as textures or material images. However, when training a CNN, usually small parts of the training images are used to ensure the computational efficiency. In this case, due to the smaller number of patches in the reconstructions, the similarity of the patch distributions is not longer clear. Therefore, we divide our training data into disjoint batches (B_j) of size $|B_j| = b$, $j = 1, \dots, N_B$ with $\bigcup_{i=1}^{N_B} B_i = \{1, \dots, m\}$. Instead of comparing the patch distributions of \tilde{x} and y_i for each i separately, we now compare the patch distribution of \tilde{x} with the distribution of all patches within the images of the batch B_i . Formally, this corresponds to replace in (4) the term

$$\frac{1}{|B_j|} \sum_{i \in B_j} W_2^2(\mu_{G_\theta(y_i)}, \mu_{\tilde{x}}) \quad \text{by} \quad W_2^2\left(\frac{1}{|B_j|} \sum_{i \in B_j} \mu_{G_\theta(y_i)}, \mu_{\tilde{x}}\right),$$

for $j = 1, \dots, N_B$. Then, we obtain the loss function

$$\mathcal{L}_{\text{WPPNet}}(\theta) = \frac{1}{|B|} \sum_{j=1}^{N_B} \frac{1}{b} \sum_{i \in B_j} \|f(G_\theta(y_i)) - y_i\|^2 + \lambda W_2^2\left(\frac{1}{b} \sum_{i \in B_j} \mu_{G_\theta(y_i)}, \mu_{\tilde{x}}\right). \quad (5)$$

We call a neural network trained with the loss function (5) a *Wasserstein Patch Prior Network* (WPPNet). Since

$$\begin{aligned} \frac{1}{|B|} \sum_{i \in B} W_2^2(\mu_{G_\theta(y_i)}, \mu_{\tilde{x}}) &= \frac{1}{|B|} \sum_{i \in B} \left(\max_{\psi \in \mathbb{R}^{\tilde{N}}} \frac{1}{N} \sum_{j=1}^N \psi^c(P_j G_\theta(y_i)) + \frac{1}{\tilde{N}} \sum_{k=1}^{\tilde{N}} \psi_k \right) \\ &\geq \max_{\psi \in \mathbb{R}^{\tilde{N}}} \frac{1}{|B|} \sum_{i \in B} \left(\frac{1}{N} \sum_{j=1}^N \psi^c(P_j G_\theta(y_i)) + \frac{1}{\tilde{N}} \sum_{k=1}^{\tilde{N}} \psi_k \right) \\ &= W_2^2\left(\frac{1}{|B|} \sum_{i \in B} \mu_{G_\theta(y_i)}, \mu_{\tilde{x}}\right), \end{aligned}$$

the loss functions (4) and (5) are related by $\mathcal{L}(\theta) \geq \mathcal{L}_{\text{WPPNet}}(\theta)$.

Remark 2. To speed up the numerical computations, we replace the empirical patch distribution $\mu_{\tilde{x}}$ of the reference image \tilde{x} by the distribution of a random subset of all

patches, i.e. we redefine $\mu_{\tilde{x}}$ as

$$\mu_{\tilde{x}} = \frac{1}{|I|} \sum_{k \in I} \delta_{P_k \tilde{x}},$$

where I is a random subset of $\{1, \dots, N\}$ of size $|I|$. For our numerical experiments we chose $|I| = 10000$.

In order to minimize the loss function (5) with a gradient-based optimization method, we need to compute the derivative of $W_2^2(\mu_{G_\theta(y)}, \mu_{\tilde{x}})$ with respect to θ for some observation $y \in \mathcal{Y}$. This can be done based on the following observations. Recall that the Wasserstein distance is given by

$$W_2^2(\mu_{G_\theta(y)}, \mu_{\tilde{x}}) = \max_{\psi \in \mathbb{R}^{\tilde{N}}} F(\psi, \theta; y), \quad F(\psi, \theta; y) := \frac{1}{N} \sum_{j=1}^N \psi^c(P_j G_\theta(y)) + \frac{1}{\tilde{N}} \sum_{k=1}^{\tilde{N}} \psi_k.$$

Then the following well-known theorem provides a connection between the gradient of the Wasserstein distance and those of F , see, e.g., [23].

Theorem 3. *Let $\theta \mapsto W_2^2\left(\frac{1}{N} \sum_{j=1}^N \delta_{P_j G_\theta(y)}, \frac{1}{\tilde{N}} \sum_{k=1}^{\tilde{N}} \delta_{P_k \tilde{x}}\right)$ and $\theta \mapsto F(\psi^*, \theta; y)$ be differentiable at θ_0 with $\psi^* \in \arg \max_{\psi} F(\psi, \theta_0; y)$. Then it holds*

$$\nabla_{\theta} W_2^2\left(\frac{1}{N} \sum_{j=1}^N \delta_{P_j G_{\theta_0}(y)}, \frac{1}{\tilde{N}} \sum_{k=1}^{\tilde{N}} \delta_{P_k \tilde{x}}\right) = \nabla_{\theta} F(\psi^*, \theta_0; y).$$

Since for almost every θ the set of minimizers

$$\sigma_{\psi}(j) = \arg \min_{k \in \{1, \dots, \tilde{N}\}} (\|P_j G_{\theta}(y) - P_k \tilde{x}\|^2 - \psi_k)$$

is single-valued, it holds that $\psi^c(P_j G_{\theta}(y)) = \|P_j G_{\theta}(y) - P_{\sigma_{\psi}(j)} \tilde{x}\|^2 - \psi_{\sigma_{\psi}(j)}$, which is differentiable in θ . Thus, by Theorem 3, the gradient of the Wasserstein-2 distance is given by

$$\nabla_{\theta} W_2^2(\mu_{G_{\theta}(y)}, \mu_{\tilde{x}}) = \nabla_{\theta} F(\psi^*, \theta; y) = \frac{2}{N} \sum_{j=1}^N (\partial_{\theta}(P_j G_{\theta}(y))^T)(P_j G_{\theta}(y) - P_{\sigma_{\psi^*}(j)} \tilde{x}), \quad (6)$$

where

$$\psi^* = \arg \max_{\psi \in \mathbb{R}^{\tilde{N}}} F(\psi, \theta; y).$$

For computing ψ^* , the authors of [23] suggest to use a (stochastic) gradient ascent.

Summarized, we obtain the following two steps.

1. Solve $\psi^* = \arg \max_{\psi \in \mathbb{R}^{\tilde{N}}} F(\psi, \theta; y)$ using a (stochastic) gradient ascent.
2. Compute $\nabla_{\theta} W_2^2(\mu_{G_{\theta}(y)}, \mu_{\tilde{x}})$ by (6).

5 Numerical Results

Next, we apply WPPNets for superresolution, i.e. we consider the inverse problem

$$y = f(x) + \eta,$$

where the forward operator f consists of a blur operator and a downsampling operator and η is some noise. Here, x denotes the high resolution ground truth and y the low resolution observation. In Subsection 5.2 and 5.3 we assume that the forward operator f is given exactly and compare the WPPNet with the methods described in Subsection 5.1. Afterwards, in Subsection 5.4, we demonstrate the robustness of WPPNets by assuming that the operator knowledge is inaccurate. Here, we generate the low-resolution data in a first example by a slightly different operator than we use for learning the WPPNet. In a second example, we consider real data, where the forward operator f is unknown. We estimate the forward operator f in a first step based on a pair of registered images. In a second step, we use this (inaccurate) estimation of the operator for reconstructing the (real) high-resolution image from the (real) low-resolution observation. Details on the architecture and the experimental setup are given in Appendix B. To evaluate the quality of our results, we use three different error measures:

- **PSNR.** The first quality measure is the peak-signal to noise ration (PSNR). For two images x and y on $[0, 1]^{m \times n}$ it is defined as

$$\text{PSNR}(x, y) = -10 \log_{10} \left(\frac{1}{mn} \|x - y\|^2 \right).$$

Consequently, larger PSNR values correspond to a better reconstruction. It is well-known that the PSNR prefers very smooth reconstructions which does not coincide with the visual impression. Therefore, we consider two further error measures.

- **Blur effect.** Second, we measure the sharpness of our results by using the so-called blur effect [8]. This metric is based on comparing an input image x with a blurred

version x_{blur} . For sharp images x , the difference should be very pronounced while it will be small for blurred x . The blur effect is normalized to $[0, 1]$, where a small blur effect indicates that x is very sharp while a large blur effect means that x is very blurry.

- **LPIPS.** Finally, we use the learned perceptual image patch similarity (LPIPS) [52]² for measuring the perceptual similarity of our results and the ground truth. The basic idea of LPIPS is to compare the feature maps extracted from some deep neural network that is trained for some classical imaging task which is not necessarily related to our original problem. A small value of LPIPS indicates a high perceptual similarity.

5.1 Comparison with Established Methods

We compare our results with several established methods from literature.

Bicubic Interpolation. The simplest comparison is the bicubic interpolation [24]. It is based on the local approximation of the image by polynomials of degree 3.

Plug-and-Play Forward Backward Splitting with DRUNet (PnP-DRUNet). Plug and Play methods were first introduced in [47]. The main idea is to consider a classical algorithm from convex optimization and replace the proximal operator with respect to the regularizer by a more general denoiser. More precisely, we modify the forward backward splitting algorithm for minimizing the function $F(x) = d(x) + R(x)$ with $d(x) = \frac{1}{2}\|f(x) - y\|^2$ given by

$$x_{r+1} = \text{prox}_{\eta R}(x_r - \eta \nabla d(x_r))$$

by the iteration

$$x_{r+1} = \mathcal{D}(x_r - \eta \nabla d(x_r)), \quad (7)$$

where \mathcal{D} is a neural network trained for denoising natural images. Here, we use the DRUNet from [51] as denoiser \mathcal{D} and run the iteration (7) for 100 iterations. Then, we set the reconstruction to be $\hat{x} = x_{100}$. It was shown in [3, 15, 19, 33, 35, 51] that Plug-and-Play methods can achieve state-of-the-art performance for several applications.

Once the denoising network is trained, computing the reconstruction of a PnP-DRUNet requires 100 computations of (7). Even though this is much faster than training a neu-

²We use the implementation <https://github.com/richzhang/PerceptualSimilarity>, version 0.1.

ral network, this is significantly slower than a simple evaluation of a neural network as required for the WPPNet.

Deep Image Prior. The idea of the Deep Image Prior (DIP) [45]³ is to solve the optimization problem

$$\hat{\theta} \in \arg \min_{\theta} \|f(G_{\theta}(z)) - y\|^2,$$

where G_{θ} is a convolutional neural network with parameters θ and z is a randomly chosen input. Then, the reconstruction \hat{x} is given by $\hat{x} = G_{\theta}(z)$. It was shown in [45], that DIP admits competitive results for many inverse problems.

Note that each reconstruction with the DIP requires the training of a neural network. Thus, the reconstruction time of DIP is much slower than for WPPNet.

CNN trained on natural images. In our numerical examples, we consider special structured images as textures and materials microstructures. A natural way to overcome the issue of missing (labeled) training data could be to train a CNN onto natural images and to hope that it generalizes to the special structured test set. Following this approach, we compare our results with an asymmetric CNN [44] trained on the 400 training images from the BSDS500 dataset [32]. As loss function, we use the standard L^2 -loss. Afterwards we apply these networks onto our special structured test set. In our results, we abbreviate this approach by CNNNat.

Training and reconstruction time of such a CNN are comparable with training and reconstruction time of a WPPNet.

Variational Wasserstein Patch Prior (WPP). The authors of [18] propose to minimize the functional (3) for reconstructing a high-resolution image x from a low-resolution observation y . It provided the original motivation of WPPNet. However, the functional (3) has to be minimized for any reconstruction which can be computationally very costly such that it is much slower than the reconstruction with WPPNet.

5.2 Texture Superresolution

First, we consider the Kylberg texture dataset [27]⁴. Here, we use the textures "Grass" and "Floor". The high-resolution ground truth and the reference image are different

³We use the original implementation from [45] available at <https://github.com/DmitryUlyanov/deep-image-prior>

⁴available at <https://kylberg.org/kylberg-texture-dataset-v-1-0>

		bicubic	PnP-DRUNet	DIP	CNNNat	WPP	WPPNet
Grass	PSNR	22.68	24.71	24.42	25.06	24.61	24.79
	Blur Effect	0.5980	0.4649	0.4316	0.4307	0.4153	0.4219
	LPIPS	0.4891	0.4074	0.2492	0.2403	0.1777	0.2353
Floor	PSNR	29.03	32.96	31.88	30.35	30.39	30.99
	Blur Effect	0.7469	0.6803	0.6613	0.5977	0.5218	0.5407
	LPIPS	0.2568	0.2584	0.1837	0.2795	0.1647	0.1705

Table 1: PSNR, Blur Effect and LPIPS value of the high-resolution reconstructions of the textures "Grass" and "Floor". The best two values are marked in bolt.

600×600 sections cropped from the original texture images. Similarly, the low-resolution training data is generated by cropping 100×100 sections from the texture images and artificially downsampling it by a predefined forward operator f . The forward operator f is a convolution with a 16×16 Gaussian blur kernel with standard deviation 2, stride 4 and $\eta \sim \mathcal{N}(0, 0.01^2)$ is some noise. To keep the dimensions consistent, we use zero-padding.

The implementation of this example is available online⁵.

Results. The resulting error measures for the textures "Grass" and "Floor" are given in Table 1 and the reconstructions are shown in Figure 2 and 3, respectively. We observe that the WPPNet and WPP result into significantly sharper and visually better results than the other methods. However, the WPP requires the minimization of the functional (3) for each reconstruction, which is computationally costly. Also the DIP requires for any reconstruction the training of a neural network and for PnP-DRUNet, we have to compute the iteration (7) several times. Thus, the reconstruction time for WPP, DIP and PnP-DRUNet is significantly larger than for WPPNet and CNNNat.

Further, we observe that PnP-DRUNet and DIP have a better PSNR value than the WPPNet for the texture "Floor". However, it is well-known that the PSNR as error measure prefers smooth images. In terms of the blur effect, LPIPS and the visual impression, the WPPNet and WPP are clearly better than the other methods.

5.3 Synchrotron Computed Tomography Data

In this subsection, we consider material data which was also used in [18, 20]. As a forward operator, we use the same f as in Section 5.2.

⁵<https://github.com/FabianAltekrueger/WPPNets>

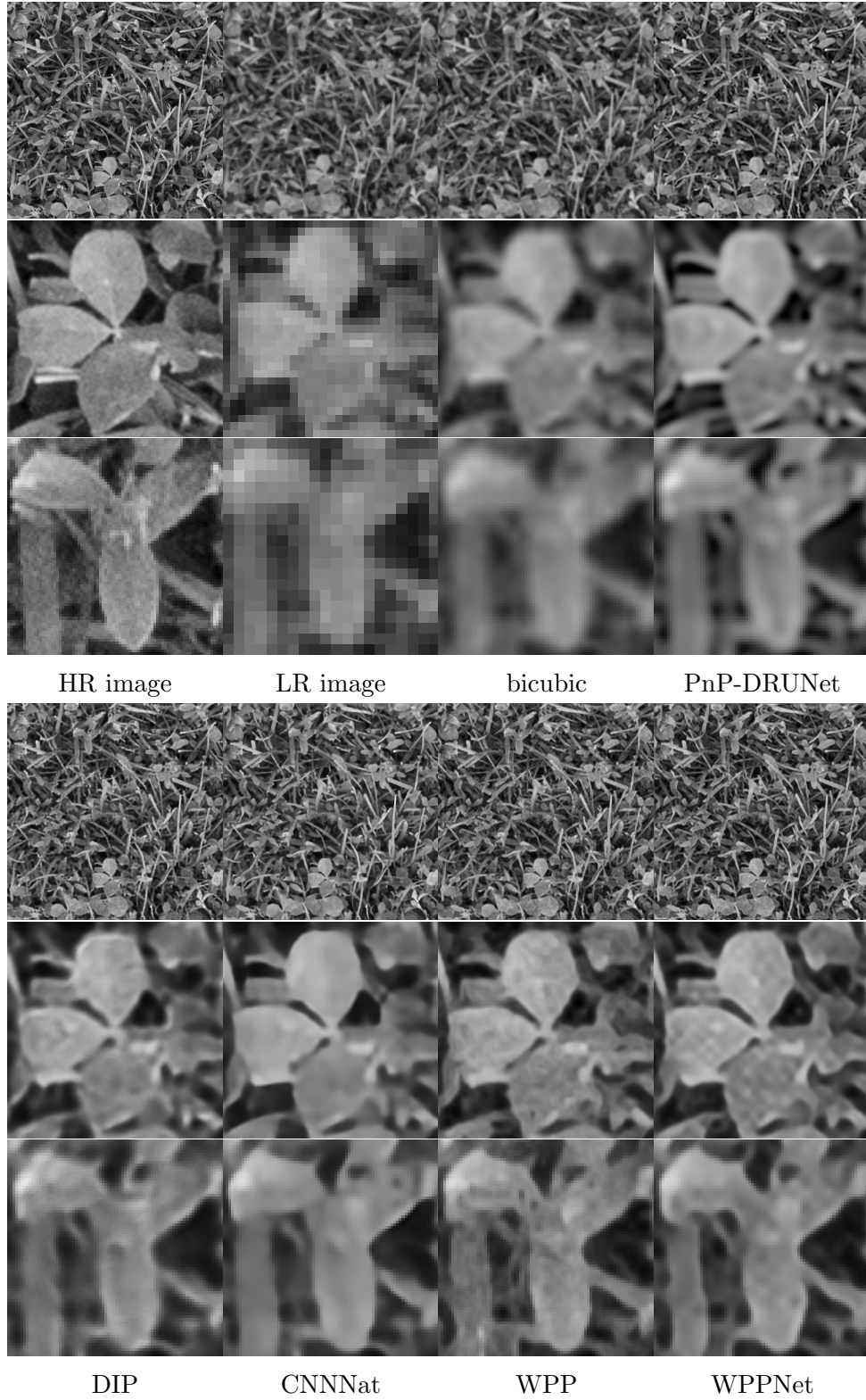


Figure 2: Reconstruction of the high resolution texture "Grass" using different methods. *Top*: full image. *Middle and bottom*: zoomed-in parts.

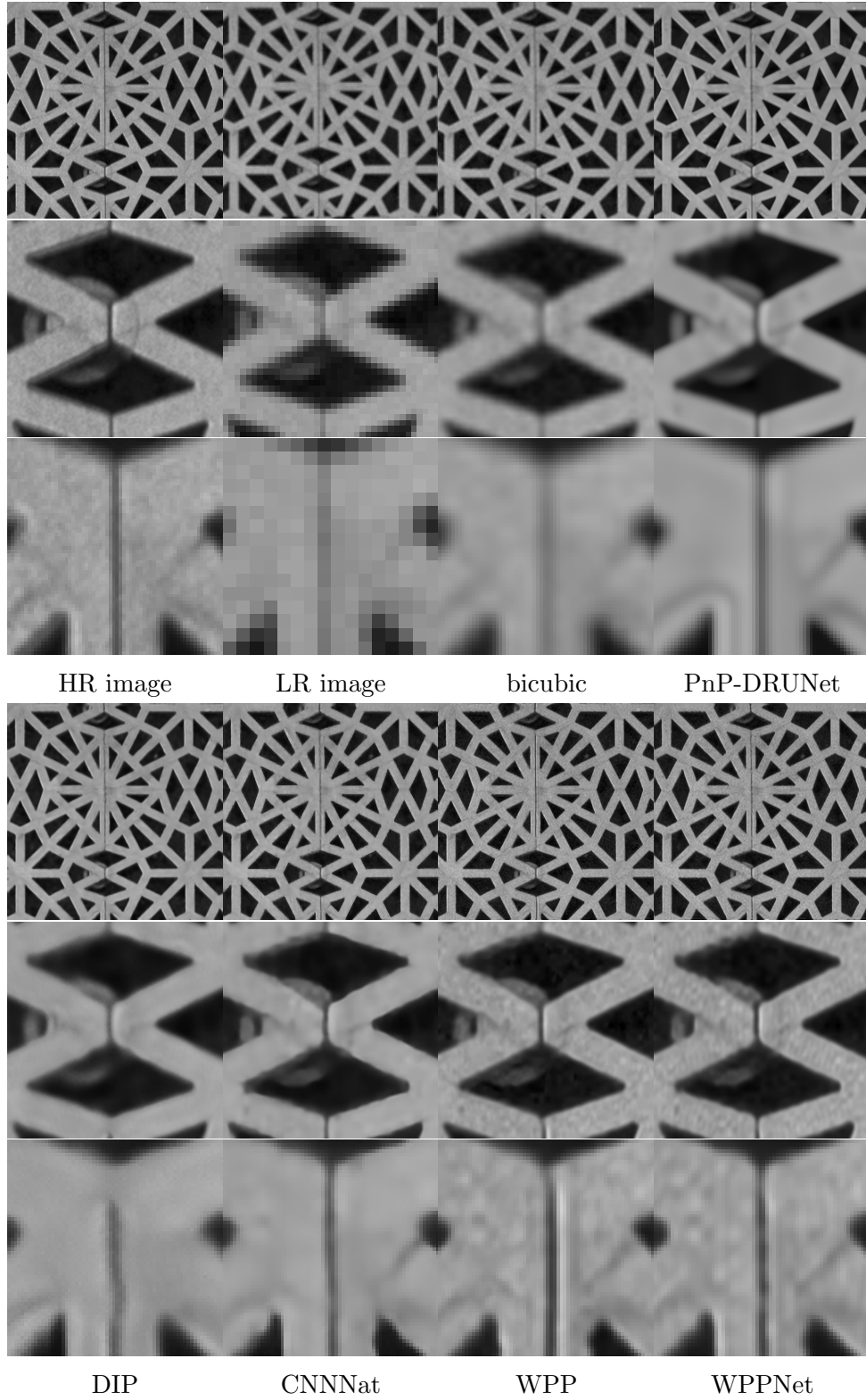


Figure 3: Reconstruction of the high resolution texture "Floor" using different methods. *Top*: full image. *Middle and bottom*: zoomed-in parts.

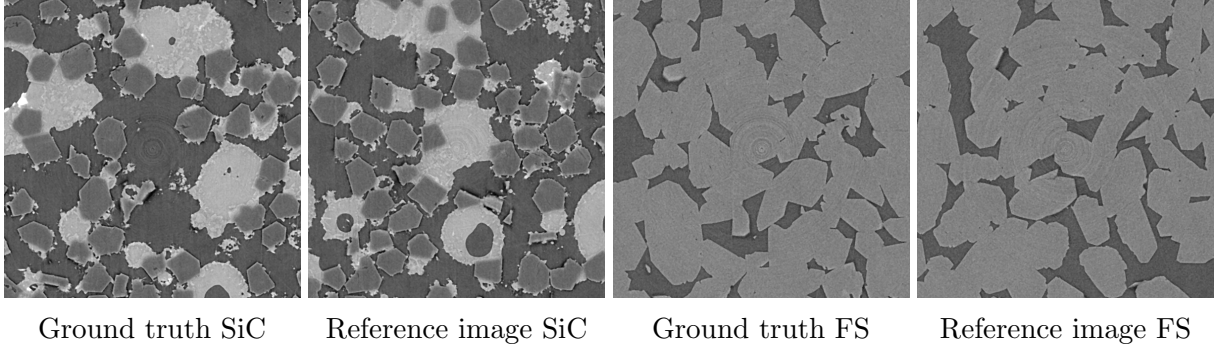


Figure 4: Ground truth and reference image used for the numerical examples.

Data generation. A series of multi-scale 3D images has been acquired by synchrotron micro-computed tomography at the SLS beamline TOMCAT. Samples of two materials were selected to provide 3D images having different levels of complexity:

- The first one is a composite ("SiC Diamonds") obtained by microwave sintering of silicon and diamonds, see [46].
- The second one is a sample of Fontainebleau sandstone ("FS"), a rather homogeneous natural rock that is commonly used in the oil industry for flow experiments.

In our experiments we consider a voxel spacing of $1.625 \mu\text{m}$. From this 3D image we extract 2D slices of size 600×600 and use them as ground truth and reference images for our experiments. Some examples are given in Figure 4. Since we require that the forward operator f is known, we generate the low resolution images artificially by extracting 2D slices from our 3D image and downsample it using the known predefined forward operator f . In this way we generate a set of 1000 low-resolution images of size 25×25 for training the WPPNet.

Results. The resulting error measures are given in Table 2 and the reconstructions are shown in Figure 5 and 6. Similar as in Subsection 5.2, we observe that the reconstructions with WPPNet and WPP are significantly sharper and visually better than the other methods. Again, the PSNR prefers in some cases the much smoother reconstructions of DIP and CNNNat. However, the results of WPPNet and WPP look visually much better which is also quantified by smaller values for LPIPS and blur effect.

We apply all methods onto a larger test set in Appendix C.

Higher Magnification Factor. Additionally to the previous examples, we apply WPP-Nets for superresolution with a magnification factor of 6 onto the SiC Diamonds image.

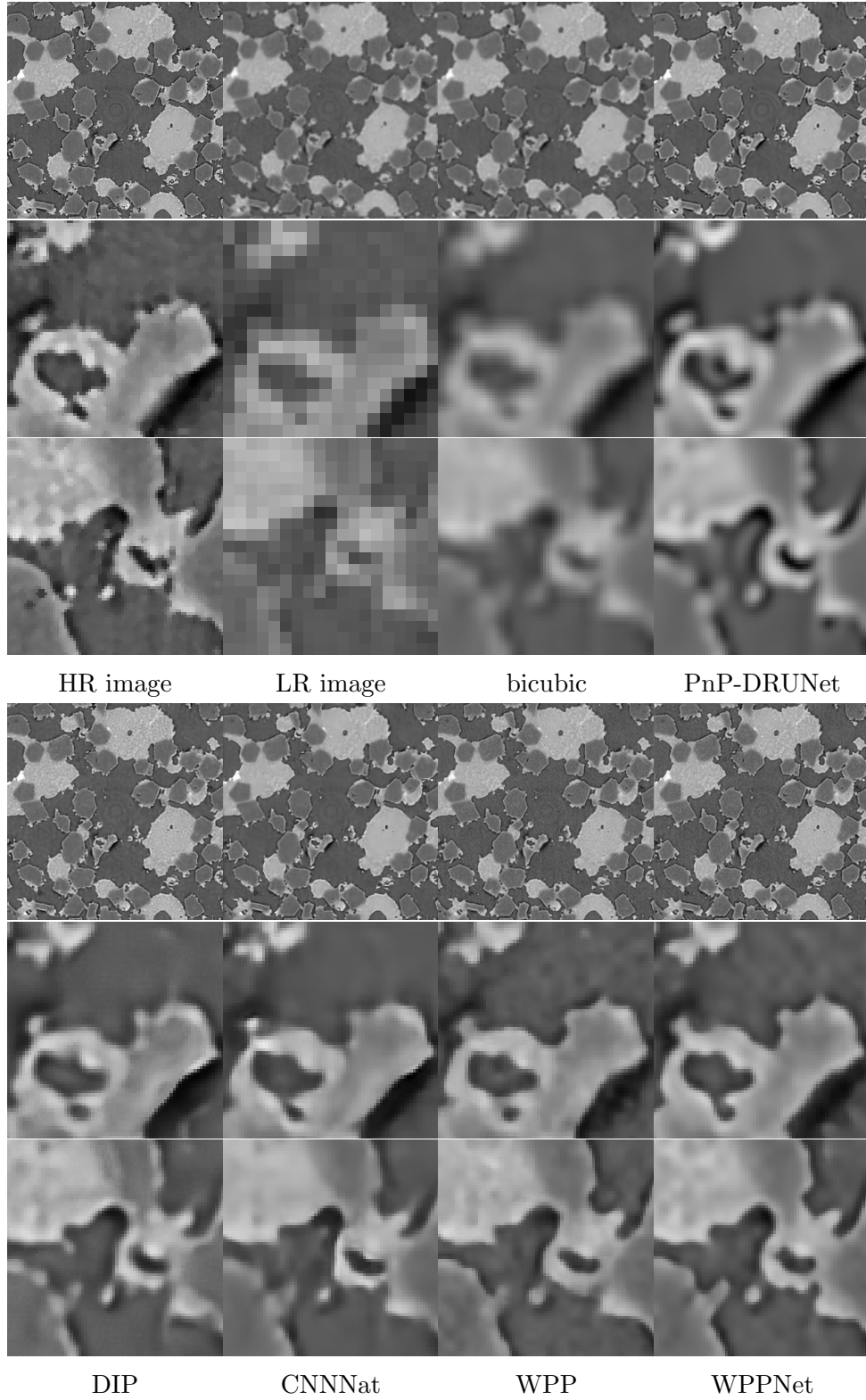


Figure 5: Reconstruction of the high resolution image "SiC Diamonds" using different methods. *Top*: full image. *Middle and bottom*: zoomed-in parts.

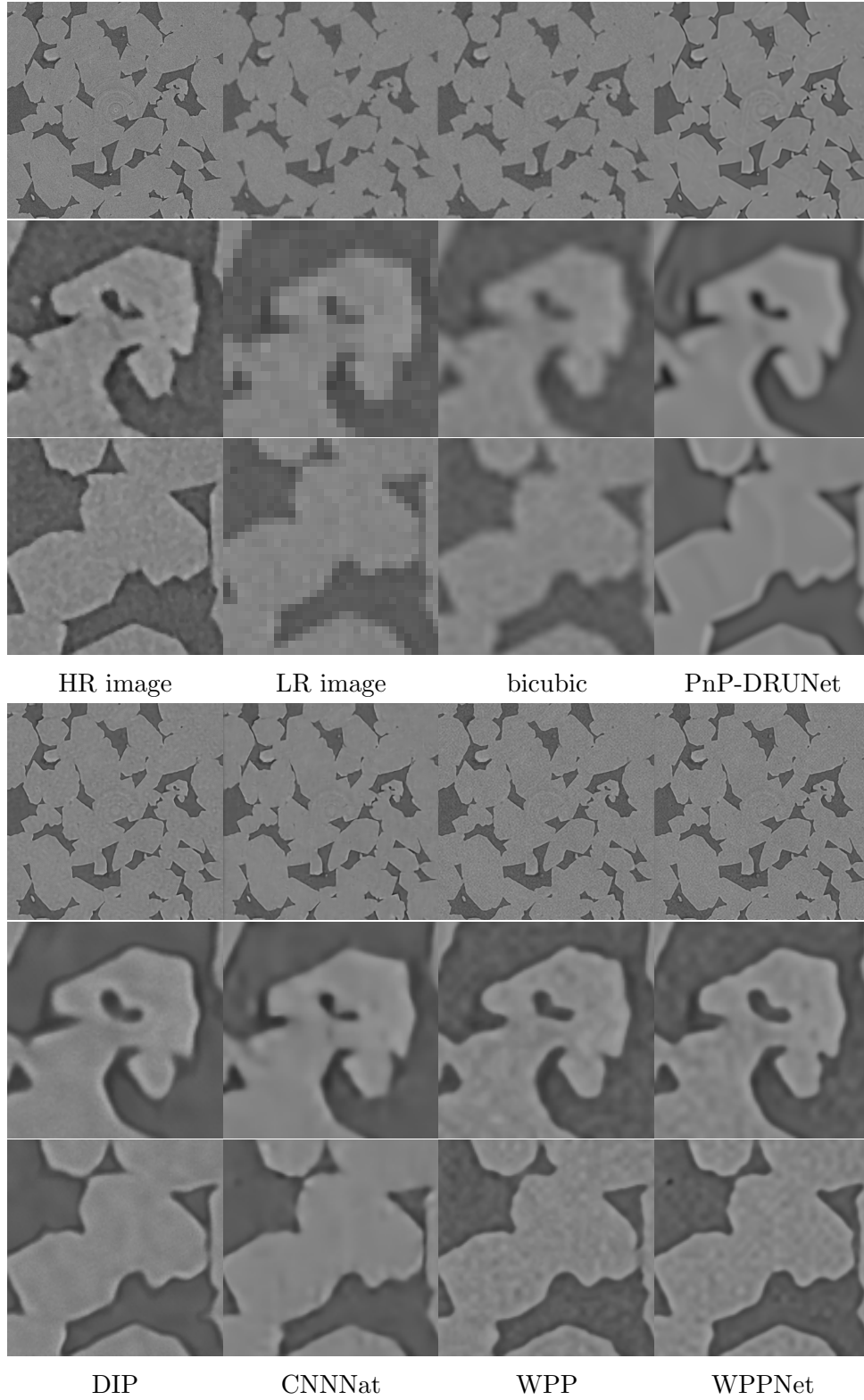


Figure 6: Reconstruction of the high resolution image "Fontainebleau sandstone" using different methods. *Top*: full image. *Middle and bottom*: zoomed-in parts.

		bicubic	PnP-DRUNet	DIP	CNNNat	WPP	WPPNet
SiC	PSNR	25.34	27.43	27.25	27.66	27.57	27.83
	Blur Effect	0.5794	0.4405	0.3829	0.4076	0.3743	0.3810
	LPIPS	0.4216	0.3133	0.1987	0.2441	0.1627	0.1819
FS	PSNR	29.19	31.05	31.18	31.68	31.07	30.85
	Blur Effect	0.4856	0.4936	0.3698	0.4276	0.3225	0.3299
	LPIPS	0.3524	0.3565	0.2230	0.2441	0.1630	0.1771

Table 2: PSNR, Blur Effect and LPIPS value of the high-resolution reconstructions. The best two values are marked in bolt.

Here, the forward operator f is given by a convolution with a 16×16 Gaussian blur kernel with standard deviation 3, stride 6 and zero-padding of width 6. As before, we set the noise to $\eta \sim \mathcal{N}(0, 0.01^2)$. We use the same ground truth and reference image as before, illustrated in Figure 4. The resulting error measures are given in Table 3 and the reconstructions are shown in Figure 7.

5.4 Stability under Inaccurate Operators

Within this subsection, we demonstrate the robustness of WPPNets against inaccurate knowledge of the forward operator f . Our data is given by the SiC Diamonds image as described in the previous subsection. In a first example, we generate the low resolution images y by using a different superresolution operator than for the training of the WPPNet and its comparisons. Second, we consider the case where the true forward operator is estimated from data. This leads by construction to a perturbed forward operator.

5.4.1 Inaccurate Forward Operator

In this example, we generate the low-resolution observations using the forward operator f_{true} given by a strided convolution with a 16×16 Gaussian blur kernel with standard deviation 2, stride 4 and zero padding as in the previous subsection. On the other hand,

		bicubic	PnP-DRUNet	DIP	CNNNat	WPP	WPPNet
SiC	PSNR	22.98	24.36	23.99	24.20	24.51	24.44
	Blur Effect	0.6875	0.6139	0.4092	0.4476	0.4081	0.4151
	LPIPS	0.5988	0.4987	0.3600	0.3306	0.2497	0.2626

Table 3: PSNR, Blur Effect and LPIPS value of the high-resolution reconstructions with magnification factor 6. The best two values are marked in bolt

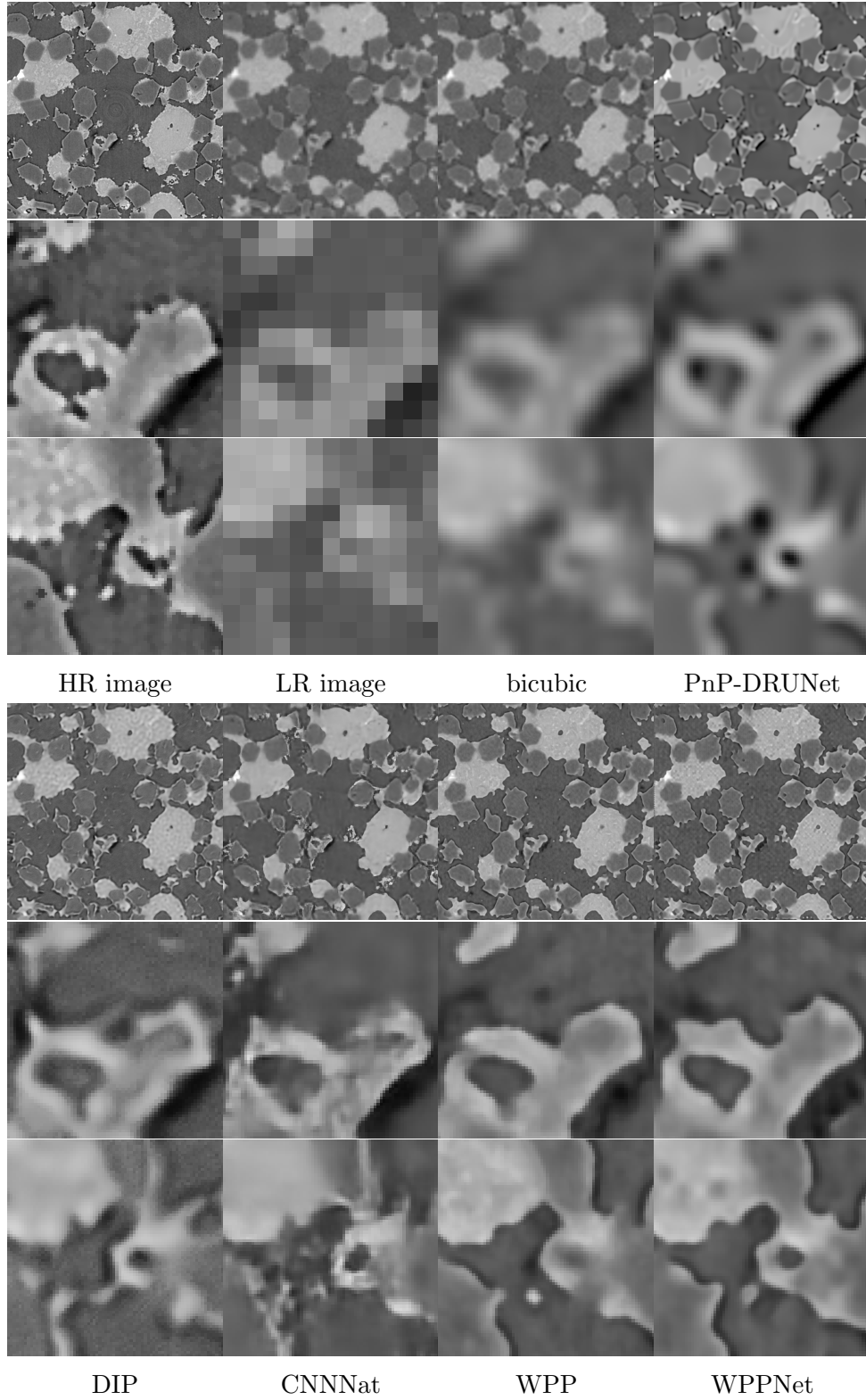


Figure 7: Reconstruction of the high resolution image "SiC Diamonds" with a magnification factor 6. *Top*: full image. *Middle and bottom*: zoomed-in parts.

		PnP-DRUNet	DIP	CNNNat	WPP	WPPNet
SiC	PSNR	26.58	25.19	23.29	27.45	27.68
	Blur Effect	0.4367	0.3678	0.3054	0.3876	0.3964
	LPIPS	0.3563	0.2471	0.2495	0.1725	0.2055

Table 4: PSNR, Blur Effect and LPIPS value of the high-resolution reconstructions with an inaccurate forward operator. The best two values are marked in bolt.

we train the WPPNet and CNNNat with an inaccurate forward operator f_{inacc} , which we also use for the reconstruction with DIP, PnP-DRUNet and WPP. The operator f_{inacc} is given in the same way as f_{true} with the only difference, that we use a standard deviation of 2.5 instead of standard deviation 2 within the Gaussian blur kernel.

The resulting error measures are given in Table 4. Further, the reconstructions using the different methods are given in Figure 8. We observe that WPPNet and WPP are much more robust against the inaccurate operator than all of the comparison methods. While the inaccurate operator leads in DIP and CNNNat to unnatural artifacts, it effects a significant blur within the PnP-DRUNet reconstructions. On the other hand, the reconstruction using WPPNet or WPP is still close to the results using the accurate operator from the previous section. Note that CNNNat and DIP have a very small blur effect. However, this is due to the fact that the reconstruction with CNNNat and DIP contains a large number of high-frequency artifacts.

5.4.2 Estimated Forward Operator

Finally, we aim to evaluate the performance of WPPNets in a real-world setting motivated by the imaging of material microstructures. We assume that we have scanned a large area from a materials microstructure using a low resolution. Due to the limited amount of time and resources it is not possible to scan the same area with a higher resolution. On the other hand, we assume that we are given a high-resolution image of some small part of this area.

In this setting, we aim to generate a high-resolution correspondence for the whole low-resolution image. We proceed in two steps. First, we estimate the forward operator of the superresolution problem using the small high-resolution part. Second, we reconstruct the high-resolution image using the estimated forward operator.

Data generation. We consider the synchrotron-computed tomography data from Section 5.3 and consider the images with voxel spacings 1.625 μm and 3.25 μm .

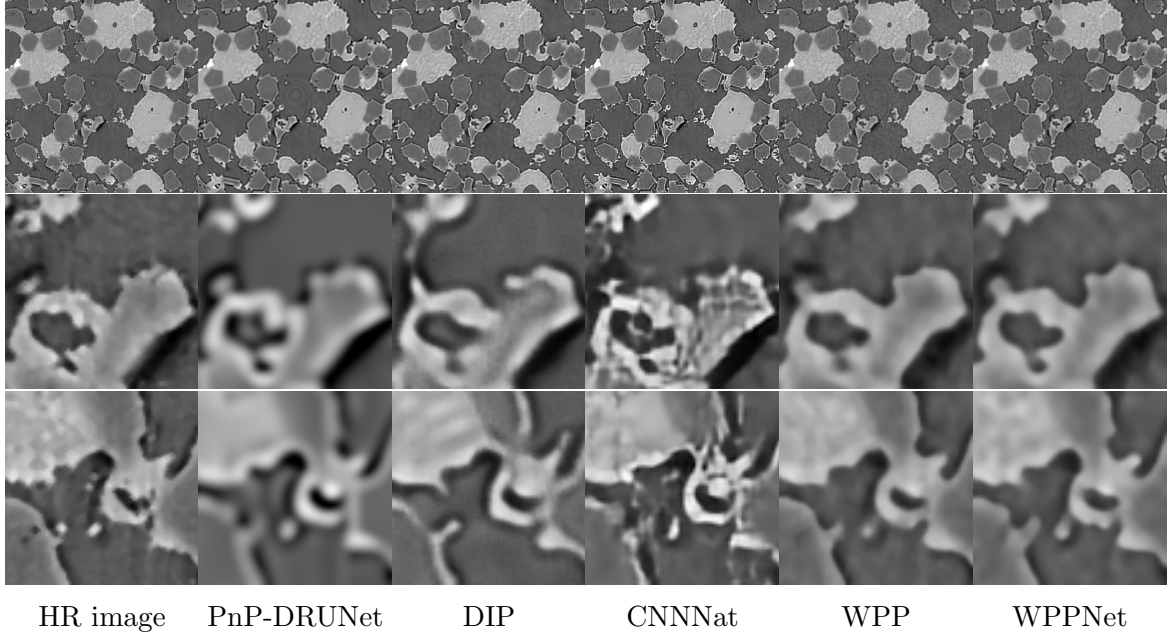


Figure 8: Reconstruction of the high resolution image "SiC Diamonds" using an inaccurate forward operator. *Top*: full image. *Middle and bottom*: zoomed-in parts.

Here, we extract a large database of low-resolution images (2D slices of the image with voxel spacing $3.25 \mu\text{m}$). Further, we extract two pairs $(\tilde{x}_1, \tilde{y}_1)$ and $(\tilde{x}_2, \tilde{y}_2)$ of 2D-slices from the images with voxel spacings $1.625 \mu\text{m}$ and $3.25 \mu\text{m}$ showing the same area of the material. Here, the \tilde{x}_i are extracted from the image with voxel spacing $1.625 \mu\text{m}$ and the \tilde{y}_i come from the image with voxel spacing $3.25 \mu\text{m}$. The pair $(\tilde{x}_1, \tilde{y}_1)$ will be used for estimating the operator and the image \tilde{x}_1 will serve as a reference image for WPPNet and WPP. Further, we use the pair $(\tilde{x}_2, \tilde{y}_2)$ for evaluating our results, where \tilde{y}_2 is the low-resolution observation, while \tilde{x}_2 is the high-resolution ground truth.

Note that $(\tilde{x}_i, \tilde{y}_i)$ are real-world data. Thus, we register the images $(\tilde{x}_i, \tilde{y}_i)$ in a pre-processing step using the scale-invariant feature transform (SIFT) [31].

In practice, the forward operator could also be estimated from synthetic data (see e.g. [18]), which circumvents the need of the given registered pairs $(\tilde{x}_i, \tilde{y}_i)$. However, generating synthetic data for the synchrotron-computed tomography data is out of scope of our paper.

Estimation of the Forward Operator. We estimate the forward operator from the registered pair $(\tilde{x}_1, \tilde{y}_1)$ in the same way as proposed in [18]. For completeness, we describe this procedure in Appendix D.

		bicubic	PnP-DRUNet	DIP	CNNNat	WPP	WPPNet
FS	PSNR	17.67	32.91	31.73	32.97	32.68	32.80
	Blur Effect	0.4817	0.4964	0.3693	0.4248	0.3330	0.3197
	LPIPS	0.2805	0.3459	0.2741	0.2882	0.1362	0.1411

Table 5: PSNR, Blur Effect and LPIPS value of the high-resolution reconstructions using the estimated forward operator. The best two values are marked in bolt.

Results. The resulting error measures are given in Table 5 and the reconstructions are shown in Figure 9. We observe that WPPNet and WPP produce significantly sharper and visually better results than the comparisons. This is also captured by the error measures. Note, that there is a change of contrast and brightness between the high-resolution and the low-resolution image. As the bicubic interpolation does not consider the operator, this results in a brightness difference of the bicubic interpolation to the ground truth.

6 Conclusion

In this paper we introduced WPPNets, which are CNNs trained with a new loss function based on comparisons of empirical patch distributions via the Wasserstein-2 distance. We demonstrated the performance of the Wasserstein patch prior networks for numerical examples and observed that they are very stable under inaccurate operators as e.g. in real-world applications.

WPPNets could be extended in several directions. First, we focused within this paper on image superresolution. However, WPPNets can be applied for any inverse problem. Further, we want to extend WPPNets for uncertainty quantification, e.g. by choosing invertible architectures [1, 4, 10, 17] or generative approaches [34, 42]. Finally, images of materials microstructures are often three-dimensional. Thus, in the future, we would extend the architecture of the WPPNets for three-dimensional images.

Acknowledgements

Funding by German Research Foundation (DFG) within the project STE 571/16-1 and by the DFG excellence cluster Math+ within the project TP: EF3-7 are gratefully acknowledged. The data from Section 5.3 and the second example in Section 5.4 has been acquired in the frame of the EU Horizon 2020 Marie Skłodowska-Curie Actions Innovative Training Network MUMMERING (MULTiscale, Multimodal and Multidimensional

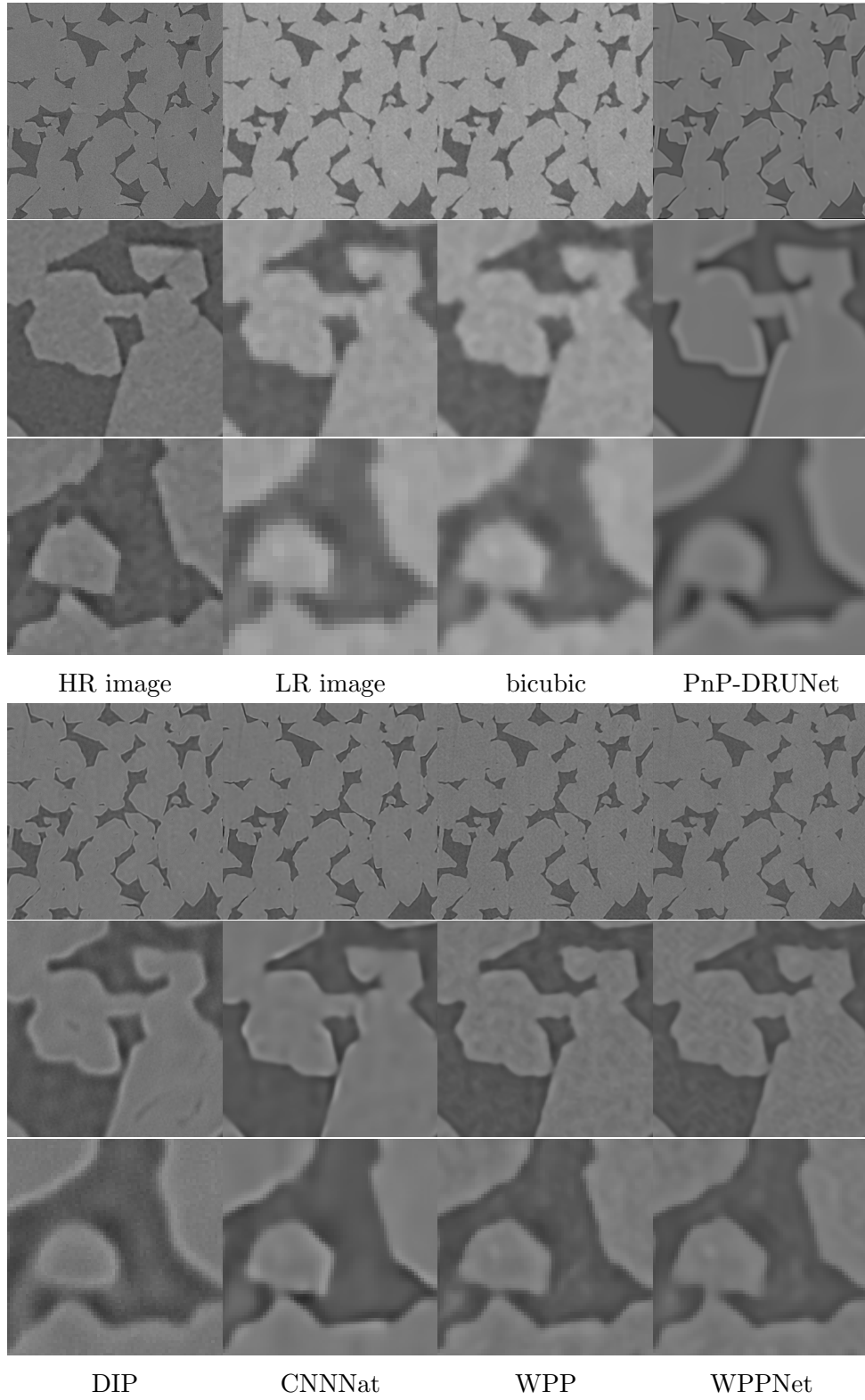


Figure 9: Reconstruction of the high resolution image "Fontainebleau sandstone" assuming the estimated forward operator. *Top*: full image. *Middle and bottom*: zoomed-in parts.

imaging for EngineeRING, Grant Number 765604) at the beamline TOMCAT of the SLS by A. Saadaldin, D. Bernard, and F. Marone Welford. We acknowledge the Paul Scherrer Institut, Villigen, Switzerland for provision of synchrotron radiation beamtime at the TOMCAT beamline X02DA of the SLS. Many thanks to Antoine Houdard for generating Figure 1 and to Dang Phoung Lan Nguyen for registering the images from the second example in Section 5.4.

A Proof of Proposition 1

By (2), for each $x \in \mathbb{R}^d$ it holds that

$$W_2^2(\mu_x, \mu_{\tilde{x}}) = \max_{\psi \in \mathbb{R}^M} \left(\frac{1}{N} \sum_{j=1}^N \psi^c(P_j x) + \frac{1}{M} \sum_{k=1}^M \psi_k \right) \geq \frac{1}{N} \sum_{j=1}^N \min_{k \in \{1, \dots, M\}} \|P_j x - P_k \tilde{x}\|_2^2,$$

using $\psi = 0$. Now, let $\sigma(j, x) \in \{1, \dots, M\}$ be one element of $\arg \min_{k \in \{1, \dots, M\}} (\|P_j x - P_k \tilde{x}\|_2^2)$ for $x \in \mathcal{X}$ and $j \in \{1, \dots, N\}$. Moreover, let $j^*(x) \in \arg \max_{j \in \{1, \dots, N\}} \|P_j x\|_\infty$ be a patch which contains the entry of x with the largest absolute value. Then we have

$$\begin{aligned} W_2^2(\mu_x, \mu_{\tilde{x}}) &\geq \frac{1}{N} \sum_{j=1}^N \|P_j x - P_{\sigma(j, x)} \tilde{x}\|_2^2 \\ &\geq \frac{1}{N} \|P_{j^*(x)} x - P_{\sigma(j^*(x), x)} \tilde{x}\|_2^2 = \frac{1}{N} \sum_{l=1}^p ((P_{j^*(x)} x)_l - (P_{\sigma(j^*(x), x)} \tilde{x})_l)^2, \end{aligned}$$

where p is the patch size. By considering just the summand l with $(P_{j^*(x)} x)_l = \|x\|_\infty$ and using that $(P_{\sigma(j^*(x), x)} \tilde{x})_l \leq \|\tilde{x}\|_\infty$, we obtain

$$W_2^2(\mu_x, \mu_{\tilde{x}}) \geq \frac{1}{N} (\max(\|x\|_\infty - \|\tilde{x}\|_\infty, 0))^2 \geq \frac{1}{N} (\max(c\|x\|_2 - \|\tilde{x}\|_\infty, 0))^2,$$

for some $c > 0$. Now define the compact set $K = \{x \in \mathcal{X} : \|x\|_2 \leq \frac{4}{c} \|\tilde{x}\|_\infty\}$. Then, it holds for all $x \in \mathcal{X} \setminus K$ that

$$(\max(c\|x\|_2 - \|\tilde{x}\|_\infty, 0))^2 = (c\|x\|_2 - \|\tilde{x}\|_\infty)^2 \quad \text{and} \quad \frac{c^2}{2} \|x\|_2^2 - 2c\|x\|_2 \|\tilde{x}\|_\infty \geq 0. \quad (8)$$

We can split the integral over φ as

$$\int_{\mathcal{X}} |\varphi(x)| dx = \int_K |\varphi(x)| dx + \int_{\mathcal{X} \setminus K} |\varphi(x)| dx.$$

Since the Wasserstein-2 distance is non-negative, we have that $|\varphi(x)| \leq 1$. As K is compact, we obtain that the first summand in the above formula is finite. It remains to show that also the second summand is finite. Indeed, it holds

$$\begin{aligned} \int_{\mathcal{X} \setminus K} |\varphi(x)| dx &= \int_{\mathcal{X} \setminus K} \exp(-\rho W_2^2(\mu_x, \mu_{\tilde{x}})) dx \\ &\leq \int_{\mathcal{X} \setminus K} \exp\left(-\frac{\rho}{N} (\max(c\|x\|_2 - \|\tilde{x}\|_\infty, 0))^2\right) dx \end{aligned}$$

Since we are integrating over all x outside from K , we obtain by (8) that

$$\begin{aligned} \int_{\mathcal{X} \setminus K} |\varphi(x)| dx &\leq \int_{\mathcal{X} \setminus K} \exp\left(-\frac{\rho}{N} (c^2\|x\|_2^2 - 2c\|x\|_2\|\tilde{x}\|_\infty + \|\tilde{x}\|_\infty^2)\right) dx \\ &\leq \int_{\mathcal{X} \setminus K} \exp\left(-\frac{\rho}{2N} c^2\|x\|_2^2\right) \exp\left(-\frac{\rho}{N} \underbrace{\left(\frac{c^2}{2}\|x\|_2^2 - 2c\|x\|_2\|\tilde{x}\|_\infty\right)}_{\geq 0 \text{ by (8)}}\right) dx \\ &\leq \int_{\mathcal{X} \setminus K} \exp\left(-\frac{\rho}{2N} c^2\|x\|_2^2\right) dx < \infty. \end{aligned}$$

This finishes the proof. \square

B Implementation details of WPPNet

All experiments are implemented in PyTorch. We run them on a single NVIDIA GeForce RTX 2060 GPU with 6 GB GPU memory.

Network Architecture. We use a 16-layer CNN G_θ which is adapted from [44]. In [44] the authors propose a so-called asymmetric CNN (ACNN) for image super-resolution consisting of 23-layers. More specifically, the ACNN has a 17-layer asymmetric block, a 1-layer memory enhancement block and a 5-layer high-frequency feature enhancement block (for more details about the structure and the tasks of the individual blocks, see [44, Section III]). As stated above, we modified the proposed ACNN and take a 10-layer asymmetric block (instead of 17-layer) in order to reduce the network complexity.

Training Details. For the training of the WPPNet we use the Adam optimizer [25] with a learning rate of 0.0001. For the training process the batch size is set to 25 and the number of epochs we trained for the reconstruction image is stated in Table 6. We choose the patch size to be $p = 6$, i.e. $P_i x$ is a small sub-image of size 6×6 of an image x . The weighting λ in (5) is chosen to be $\lambda = 0.02$. To obtain an approximation of the

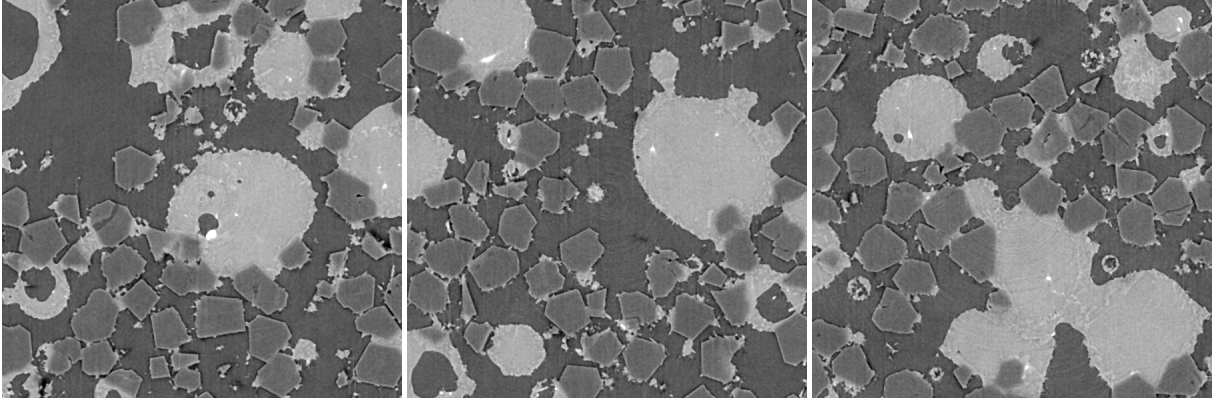


Figure 10: Exemplary ground truth images used for further numerical examples.

maximizer ψ^* of F we use 20 iterations (except for Figure 2, there we used 10 iterations) of a stochastic gradient ascent with a learning rate of 1. Moreover, instead of starting with an arbitrary ψ_k^0 or choosing $\psi_k^0 = 0$ for the optimization in epoch k , we save the approximated maximizer ψ_{k-1}^{20} from the previous epoch $k - 1$ and use it as the starting vector in epoch k , i.e. $\psi_{k-1}^{20} = \psi_k^0$. Herewith we reach a better approximation of the maximizer ψ_k^* in a computationally efficient way.

C Evaluation on a Larger Test Set

In order to make the experiments from Section 5.3 more reliable, we apply the different methods onto a larger test set. Three exemplar images from the test set are given in Figure 10. The average of the errors are given in Table 7. Again, the WPPNet and WPP perform better than the other methods in terms of the considered error measures. Overall, the results are comparable with the results from Section 5.3.

D Estimation of the Forward Operator

In the following, we describe the estimation process of the forward operator f for super-resolution, which is used in the second example of Section 5.4. For the estimation, we

	Figure 2	Figure 3	Figure 5	Figure 6	Figure 7	Figure 8	Figure 9
epochs	420	270	450	420	570	420	150

Table 6: Number of epochs to obtain the reconstructions visualized in the respective Figure.

		bicubic	PnP-DRUNet	DIP	CNNNat	WPP	WPPNet
SiC	PSNR	25.70	27.72	27.30	28.00	27.72	28.00
	Blur Effect	0.5342	0.4455	0.3802	0.3783	0.3596	0.3663
	LPIPS	0.4110	0.3265	0.2016	0.2272	0.1591	0.1830

Table 7: Averaged PSNR, Blur Effect and LPIPS value of the high-resolution reconstructions. The best two values are marked in bold.

assume that we have given a registered pair (\tilde{x}, \tilde{y}) of a high-resolution and a low-resolution image and follow the lines of [18].

We assume that our forward operator is given by $f(x) = S(k * x + b)$ for a 15×15 blur kernel k , a bias $b \in \mathbb{R}$ and a downsampling operator S .

Definition of the downsampling operator. Further, for the downsampling operator S , we make use of Fourier transforms. Given an image $x \in \mathbb{R}^{n_x, n_y}$ the two-dimensional discrete Fourier transform (DFT) is defined by $\mathcal{F}_{n_x, n_y} := \mathcal{F}_{n_x} \otimes \mathcal{F}_{n_y}$, where we have $\mathcal{F}_n = (\exp(-2\pi i k l / n))_{k, l=0}^{n-1}$. Now, the downsampling operator $S: \mathbb{R}^{m_x, m_y} \rightarrow \mathbb{R}^{n_x, n_y}$ is given by

$$S = \frac{n_x n_y}{m_x m_y} \mathcal{F}_{n_x, n_y}^{-1} D \mathcal{F}_{m_x, m_y},$$

where for $x \in \mathbb{C}^{m_x, m_y}$ the (i, j) -th entry of $D(x)$ is given by $x_{i', j'}$, where

$$i' = \begin{cases} i, & \text{if } i \leq \frac{n_x}{2}, \\ i + m_x - n_x, & \text{otherwise.} \end{cases}$$

and j' is defined analogously. Thus, the operator S generates a downsampled version $S(x)$ of an image x by removing the high-frequency part from x . Note that even if the Fourier matrix \mathcal{F}_{n_x, n_y} is complex valued, the range of S is real-valued, as D preserves Hermitian-symmetric spectra.

Estimation of Blur Kernel and Bias. We assume that we have given images $\tilde{x} \in \mathbb{R}^{m_x, m_y}$ and $\tilde{y} \in \mathbb{R}^{n_x, n_y}$ related by $\tilde{y} \approx S(k * \tilde{x} + b)$, where the blur kernel $k \in \mathbb{R}^{15 \times 15}$ and the bias $b \in \mathbb{R}$ are unknown. In the following, we aim to reconstruct k and b from \tilde{x} and \tilde{y} . Here, we use the notations $N = n_x n_y$ and $M = m_x m_y$. Further let $\tilde{k} \in \mathbb{R}^{m_x, m_y}$ be the kernel k padded with zeros such that it still corresponds to the same convolution as k , but has size $m_x \times m_y$.

Applying the DFT on both sides of $y = S(k * \tilde{x} + b) = S(\tilde{k} * \tilde{x} + b)$ and using the

definition of S , we obtain that

$$\hat{y} = \frac{N}{M} D(\hat{k} \odot \hat{x} + Mbe) = \frac{N}{M} D(\hat{k}) \odot D(\hat{x}) + Nbe,$$

where $\hat{y} = \mathcal{F}_{n_x, n_y} \tilde{y}$, $\hat{x} = \mathcal{F}_{m_x, m_y} \tilde{x}$, $\hat{k} = \mathcal{F}_{m_x, m_y} \tilde{k}$, \odot is the elementwise product and e denotes the first unit vector (i.e. $e_{0,0} = 1$ and all other entries are zero). Now, we can conclude that

$$D(\hat{k}) = \frac{M}{N} \hat{y} \oslash D(\hat{x}) - \frac{Mb}{\hat{x}_{0,0}} e,$$

where \oslash is the elementwise quotient. In practice, we stabilize this quotient by increasing the absolute value of $D(\hat{x})$ by 10^{-5} while retaining the phase. Thus, assuming that the high-frequency part of k is negligible (i.e. that $D^T Dk = k$), we can approximate \hat{k} by

$$\hat{k} \approx \frac{M}{N} D^T \hat{y} \oslash D(\hat{x}) - \frac{Mb}{\hat{x}_{0,0}} e.$$

Applying the inverse DFT this becomes

$$\tilde{k} \approx \mathcal{F}_{m_x, m_y}^{-1} \left(\frac{M}{N} D^T (\hat{y} \oslash D(\hat{x})) \right) - \frac{b}{\hat{x}_{0,0}}.$$

Using the assumption that \tilde{k} is zero outside of the 15×15 patch, where k is located, we can estimate b by taking the mean over all pixels of $\mathcal{F}_{m_x, m_y}^{-1} \left(\frac{M}{N} D^T (\hat{y} \oslash D(\hat{x})) \right)$ outside of this 15×15 patch. Afterwards, we estimate k by reprojecting

$$\mathcal{F}_{m_x, m_y}^{-1} \left(\frac{M}{N} D^T (\hat{y} \oslash D(\hat{x})) \right) - \frac{b}{\hat{x}_{0,0}}$$

to the set of all real 15×15 kernels.

References

- [1] L. Ardizzone, J. Kruse, C. Rother, and U. Köthe. Analyzing inverse problems with invertible neural networks. In *7th International Conference on Learning Representations, ICLR 2019, New Orleans, LA, USA, May 6-9, 2019*, 2019.
- [2] A. Buades, B. Coll, and J.-M. Morel. A non-local algorithm for image denoising. In *2005 IEEE Computer Society Conference on Computer Vision and Pattern Recognition*, volume 2, pages 60–65. IEEE, 2005.

- [3] S. H. Chan, X. Wang, and O. A. Elgendy. Plug-and-play ADMM for image restoration: Fixed-point convergence and applications. *IEEE Transactions on Computational Imaging*, 3(1):84–98, 2016.
- [4] R. Chen, J. Behrmann, D. K. Duvenaud, and J.-H. Jacobsen. Residual flows for invertible generative modeling. In *Advances in Neural Information Processing Systems*, volume 32. Curran Associates, Inc., 2019.
- [5] J. Cheng, Z. Han, Z. Wang, and L. Chen. “One-shot” super-resolution via backward style transfer for fast high-resolution style transfer. *IEEE Signal Processing Letters*, 28:1485–1489, 2021.
- [6] P. L. Combettes and V. R. Wajs. Signal recovery by proximal forward-backward splitting. *Multiscale Modeling & Simulation*, 4(4):1168–1200, 2005.
- [7] L. Condat, D. Kitahara, A. Contreras, and A. Hirabayashi. Proximal splitting algorithms: Relax them all. *arXiv preprint arXiv:1912.00137*, 2019.
- [8] F. Crete, T. Dolmiere, P. Ladret, and M. Nicolas. The blur effect: perception and estimation with a new no-reference perceptual blur metric. In *Human vision and electronic imaging XII*, volume 6492, page 64920I. International Society for Optics and Photonics, 2007.
- [9] K. Dabov, A. Foi, V. Katkovnik, and K. Egiazarian. Image denoising by sparse 3-d transform-domain collaborative filtering. *IEEE Transactions on Image Processing*, 16(8):2080–2095, 2007.
- [10] L. Dinh, J. Sohl-Dickstein, and S. Bengio. Density estimation using real NVP. In *5th International Conference on Learning Representations, ICLR 2017, Toulon, France, April 24-26, 2017, Conference Track Proceedings*, 2017.
- [11] C. Dong, C. C. Loy, K. He, and X. Tang. Image super-resolution using deep convolutional networks. *IEEE Transactions on Pattern Analysis and Machine Intelligence*, 38(2):295–307, 2015.
- [12] J. Eckstein and D. P. Bertsekas. On the douglas—rachford splitting method and the proximal point algorithm for maximal monotone operators. *Mathematical Programming*, 55(1):293–318, 1992.

- [13] A. Effland, E. Kobler, K. Kunisch, and T. Pock. Variational networks: An optimal control approach to early stopping variational methods for image restoration. *Journal of Mathematical Imaging and Vision*, 62(3):396, 2020.
- [14] A. A. Efros and T. K. Leung. Texture synthesis by non-parametric sampling. In *Proceedings of the seventh IEEE International Conference on Computer Vision*, volume 2, pages 1033–1038. IEEE, 1999.
- [15] H. Gupta, K. H. Jin, H. Q. Nguyen, M. T. McCann, and M. Unser. CNN-based projected gradient descent for consistent CT image reconstruction. *IEEE Transactions on Medical Imaging*, 37(6):1440–1453, 2018.
- [16] J. Gutierrez, J. Rabin, B. Galerne, and T. Hurtut. Optimal patch assignment for statistically constrained texture synthesis. In *International Conference on Scale Space and Variational Methods in Computer Vision*, pages 172–183. Springer, 2017.
- [17] P. Hagemann, J. Hertrich, and G. Steidl. Stochastic normalizing flows for inverse problems: a Markov Chains viewpoint. *ArXiv 2109.11375*, 2021.
- [18] J. Hertrich, A. Houdard, and C. Redenbach. Wasserstein patch prior for image superresolution. *arXiv preprint arXiv:2109.12880*, 2021.
- [19] J. Hertrich, S. Neumayer, and G. Steidl. Convolutional proximal neural networks and plug-and-play algorithms. *Linear Algebra and its Applications*, 631:203–234, 2021.
- [20] J. Hertrich, D. P. L. Nguyen, J.-F. Aujol, D. Bernard, Y. Berthoumieu, A. Saadaldin, and G. Steidl. PCA reduced Gaussian mixture models with applications in superresolution. *Inverse Problems & Imaging*, 2021.
- [21] A. Houdard, C. Bouveyron, and J. Delon. High-dimensional mixture models for unsupervised image denoising (HDMI). *SIAM Journal on Imaging Sciences*, 11(4):2815–2846, 2018.
- [22] A. Houdard, A. Leclaire, N. Papadakis, and J. Rabin. A generative model for texture synthesis based on optimal transport between feature distributions. *arXiv preprint arXiv:2007.03408*, 2021.
- [23] A. Houdard, A. Leclaire, N. Papadakis, and J. Rabin. Wasserstein generative models for patch-based texture synthesis. In A. Elmoataz, J. Fadili, Y. Quéau, J. Rabin, and L. Simon, editors, *Scale Space and Variational Methods in Computer Vision*, volume 12679 of *Lecture Notes in Computer Science*, pages 269–280. Springer, 2021.

- [24] R. Keys. Cubic convolution interpolation for digital image processing. *IEEE Transactions on Acoustics, Speech, and Signal Processing*, 29(6):1153–1160, 1981.
- [25] D. P. Kingma and J. Ba. Adam: A method for stochastic optimization. In *International Conference on Learning Representations*, 2015.
- [26] E. Kobler, A. Effland, K. Kunisch, and T. Pock. Total deep variation for linear inverse problems. In *Proceedings of the IEEE/CVF Conference on Computer Vision and Pattern Recognition*, pages 7549–7558, 2020.
- [27] G. Kylberg. *The Kylberg texture dataset v. 1.0*. Centre for Image Analysis, Swedish University of Agricultural Sciences and Uppsala University, 2011.
- [28] M. Lebrun, A. Buades, and J.-M. Morel. A nonlocal Bayesian image denoising algorithm. *SIAM Journal on Imaging Sciences*, 6(3):1665–1688, 2013.
- [29] A. Leclaire and J. Rabin. A fast multi-layer approximation to semi-discrete optimal transport. In *International Conference on Scale Space and Variational Methods in Computer Vision*, pages 341–353. Springer, 2019.
- [30] B. Lim, S. Son, H. Kim, S. Nah, and K. Mu Lee. Enhanced deep residual networks for single image super-resolution. In *Proceedings of the IEEE Conference on Computer Vision and Pattern Recognition workshops*, pages 136–144, 2017.
- [31] D. G. Lowe. Object recognition from local scale-invariant features. In *Proceedings of the seventh IEEE International Conference on Computer Vision*, volume 2, pages 1150–1157. IEEE, 1999.
- [32] D. Martin, C. Fowlkes, D. Tal, and J. Malik. A database of human segmented natural images and its application to evaluating segmentation algorithms and measuring ecological statistics. In *Proceedings of the International Conference on Computer Vision*, volume 2, pages 416–423, July 2001.
- [33] T. Meinhardt, M. Moller, C. Hazirbas, and D. Cremers. Learning proximal operators: Using denoising networks for regularizing inverse imaging problems. In *Proceedings of the IEEE International Conference on Computer Vision*, pages 1781–1790, 2017.
- [34] M. Mirza and S. Osindero. Conditional generative adversarial nets. *arXiv preprint arXiv:1411.1784*, 2014.

- [35] S. Ono. Primal-dual plug-and-play image restoration. *IEEE Signal Processing Letters*, 24(8):1108–1112, 2017.
- [36] S. Parameswaran, C. Deledalle, L. Denis, and T. Q. Nguyen. Accelerating GMM-based patch priors for image restoration: Three ingredients for a 100x speed-up. *IEEE Transactions on Image Processing*, 28(2):687–698, 2019.
- [37] Y. Romano, M. Elad, and P. Milanfar. The little engine that could: Regularization by denoising (RED). *SIAM Journal on Imaging Sciences*, 10(4):1804–1844, 2017.
- [38] Y. Romano, J. Isidoro, and P. Milanfar. RAISR: Rapid and accurate image super resolution. *IEEE Transactions on Computational Imaging*, 3(1):110–125, 2017.
- [39] C. Saharia, J. Ho, W. Chan, T. Salimans, D. J. Fleet, and M. Norouzi. Image super-resolution via iterative refinement. *arXiv preprint arXiv:2104.07636*, 2021.
- [40] P. Sandeep and T. Jacob. Single image super-resolution using a joint GMM method. *IEEE Transactions on Image Processing*, 25(9):4233–4244, 2016.
- [41] A. Shocher, N. Cohen, and M. Irani. “Zero-shot” super-resolution using deep internal learning. In *Proceedings of the IEEE Conference on Computer Vision and Pattern Recognition*, pages 3118–3126, 2018.
- [42] K. Sohn, H. Lee, and X. Yan. Learning structured output representation using deep conditional generative models. *Advances in neural information processing systems*, 28:3483–3491, 2015.
- [43] Y. Sun, B. Wohlberg, and U. S. Kamilov. An online plug-and-play algorithm for regularized image reconstruction. *IEEE Transactions on Computational Imaging*, 5(3):395–408, 2019.
- [44] C. Tian, Y. Xu, W. Zuo, C.-W. Lin, and D. Zhang. Asymmetric cnn for image superresolution. *IEEE Transactions on Systems, Man, and Cybernetics: Systems*, 2021.
- [45] D. Ulyanov, A. Vedaldi, and V. Lempitsky. Deep image prior. In *Proceedings of the IEEE Conference on Computer Vision and Pattern Recognition*, pages 9446–9454, 2018.
- [46] S. Vaucher, P. Unifantowicz, C. Ricard, L. Dubois, M. Kuball, J.-M. Catala-Civera, D. Bernard, M. Stampanoni, and R. Nicula. On-line tools for microscopic and

- macroscopic monitoring of microwave processing. *Physica B: Condensed Matter*, 398(2):191–195, 2007.
- [47] S. V. Venkatakrisnan, C. A. Bouman, and B. Wohlberg. Plug-and-play priors for model based reconstruction. In *2013 IEEE Global Conference on Signal and Information Processing*, pages 945–948. IEEE, 2013.
 - [48] X. Wang, K. Yu, S. Wu, J. Gu, Y. Liu, C. Dong, Y. Qiao, and C. Change Loy. ESRGAN: Enhanced super-resolution generative adversarial networks. In *Proceedings of the European Conference on Computer Vision (ECCV) workshops*, pages 0–0, 2018.
 - [49] Y. Wang, Q. Yao, J. T. Kwok, and L. M. Ni. Generalizing from a few examples: A survey on few-shot learning. *ACM Computing Surveys*, 53(3), 2020.
 - [50] Z. Wang, J. Chen, and S. C. Hoi. Deep learning for image super-resolution: A survey. *IEEE Transactions on Pattern Analysis and Machine Intelligence*, 2020.
 - [51] K. Zhang, Y. Li, W. Zuo, L. Zhang, L. Van Gool, and R. Timofte. Plug-and-play image restoration with deep denoiser prior. *IEEE Transactions on Pattern Analysis and Machine Intelligence*, 2021.
 - [52] R. Zhang, P. Isola, A. A. Efros, E. Shechtman, and O. Wang. The unreasonable effectiveness of deep features as a perceptual metric. In *Proceedings of the IEEE Conference on Computer Vision and Pattern Recognition*, pages 586–595, 2018.
 - [53] Y. Zhang, Y. Tian, Y. Kong, B. Zhong, and Y. Fu. Residual dense network for image super-resolution. In *Proceedings of the IEEE Conference on Computer Vision and Pattern Recognition*, pages 2472–2481, 2018.
 - [54] D. Zoran and Y. Weiss. From learning models of natural image patches to whole image restoration. In *IEEE International Conference on Computer Vision*, pages 479–486. IEEE, 2011.